JOURNAL OF MATERIALS SCIENCE **40** (2005) 429–439

Microscale testing of the strut in open cell aluminum foams

J. ZHOU, S. ALLAMEH, W. O. SOBOYEJO
Princeton Materials Institute and The Department of Mechanical and Aerospace Engineering, Princeton University, Olden Street, Princeton, NJ 08540, USA
E-mail: soboyejo@princeton.edu

This paper presents the results of micro-tensile testing of the individual struts that were extracted from open cell aluminum foams in the as-fabricated (F), annealed (O) and T6-strengthened (T6) conditions. The results reveal that foam struts are generally stronger and more dutile than the corresponding solid alloys under the same heat treatment conditions. The distinguished strut properties are attributed to the unique grain structures of the struts typically consisting of one grain or having bamboo-like grain structure. The measured strut strengths are also incorporated into mechanics models to estimate foam strengths. A comparison of the predicted and measured foam strengths shows that direct measurement of strut properties is critical to make precise estimation of foam strengths.

1. Introduction

The mechanical properties of open cell metallic foams have been shown to depend strongly on the properties of the foam struts [1–7]. For example, the plastic collapse strength, $\sigma_{\mathrm{pl}}^{\mathrm{cl}}$, of a foam is a function of the strut yield strength, σ_{YS}, as well as its relative density:

$$\frac{\sigma_{\mathrm{pl}}^{\mathrm{cl}}}{\sigma_{\mathrm{YS}}} = C_1\left(\frac{\rho_{\mathrm{f}}}{\rho_{\mathrm{s}}}\right)^{\frac{3}{2}} \tag{1}$$

where ρ_{f} and ρ_{s} are the densities of a foam block and bulk/fully dense solid alloy from which the foam is fabricated respectively; C_1 is a constant accounting for the variation in cell structure, which can be determined readily from experimental results [1]. Although Equation 1 indicates the strong dependence of foam strengths on strut strengths, most estimates of foam strengths utilize the nominal strengths of the corresponding bulk alloys from which foams are fabricated. However, the strengths of the bulk alloys may be significantly different from the struts, due largely to the microstructure and composition differences between struts and the corresponding bulk alloy. The differences are caused by foam fabrication processes [8–11].

Nevertheless, there have been relatively few studies of strut mechanical properties [11–15]. Simon and Gibson [12] found that there were a large number of non-uniformly distributed particles in the cell walls of closed cell foams, and the volume fractions of these particles ranged from 10 to 50%. They also estimated the yield strengths of cell wall materials from the measured microhardness using approximate relationship, $\sigma_{\mathrm{YS}} = \mathit{Hardness}/3$. The results showed that the estimated yield strengths of the cell walls could be significantly different from the nominal strength. Zhou *et al.* [13] found that the average values of the strut microhardness were about twice those of the corresponding bulk alloy subjected to the same annealing process. However, microhardness testing provides only approximate estimates of strut strengths in selected regions. Furthermore, a comparison between the measured and predicted foam strength suggested that the measured strengths of the annealed Duocel® open cell aluminum foams are generally stronger than the predictions from the model using the nominal strength of the corresponding fully-dense alloy [13]. There is, therefore, a need for direct measurements of strut mechanical properties.

In this paper, a micro-tensile testing technique, developed originally for the testing of micro-electromechanical systems (MEMS) [16], is used for measurements of strut mechanical properties. Following extraction of individual struts from aluminum foams using electrodischarged machining (EDM), micro-tensile tests were performed on struts in the as-fabricated (F), annealed (O) and T6-strengthened (T6) conditions. The measured strut strengths were then compared with those obtained from the fully dense 6101 aluminum subjected to the same heat treatment conditions. The strut strengths were also incorporated into the Gibson-Ashby model [1] and a four-strut unit cell model [7]. The measured strut properties are shown to be critical for accurate foam strength estimation.

2. Duocel® open cell Al foams and processing

Duocel® open cell aluminum foams were fabricated from the 6101 aluminum alloy be ERG, Oakland CA, using a casting method described by Ashby *et al.* [8]. Typical open cell morphology is shown in Fig. 1. The pore density of this foam is 10 pores per inch (PPI)

TABLE I Chemical compositions of bulk 6101 casting alloy (in weight percent)

Samples	Cu	Mg	Mn	Si	Fe	Zn	B	Others	Al
		0.35		0.30					
Nominal	0.10		0.03		0.50	0.10	0.06	0.10	
		–		–					Balance
Composition	max		max		max	max	max	max	
		0.80		0.70					
Bulk alloy	0.04	0.47	0.02	0.29	0.18	0.01	0.04	–	98.93
Foam	0.03	0.29	0.01	0.25	0.14	0.01	0.03	–	99.22

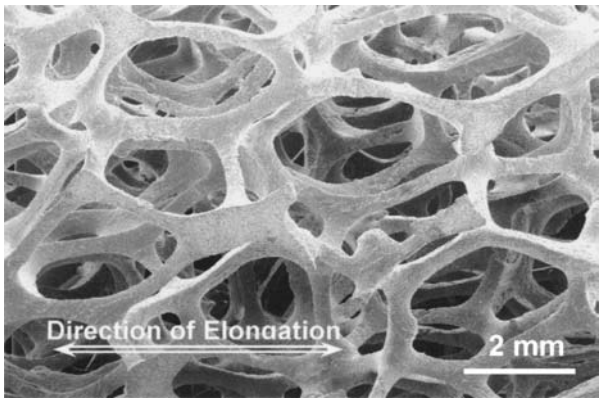

Figure 1 Typical morphology of a Duocel® open cell 6101 aluminum foam. The pore density of the shown foam is 10 pores per inch (PPI). The cells are elongated along the directions as indicated by the double-direction arrow.

corresponding to 4 pores per centimeter. The chemical compositions of the foams and the bulk alloy were analyzed using the ICP-atomic emission technique. The results are presented in Table I [13]. For a comparison, the nominal chemical composition of the 6101 aluminum alloy [17] is also presented in Table I. The chemical composition of the bulk alloy is essentially consistent with the nominal chemical composition. However, the percentages of the major alloying elements in the foams are clearly lower than those in the corresponding bulk alloy.

After fabrication, the as-fabricated foams were annealed or strengthened using T6 process. The T6-strengthening process involved solution treatment at 527°C for 8 h, prior to water quenching and ageing at 177°C for 8 h. The annealing treatment involved heat treatment at 412°C for 3 h, prior to a two-step cooling to room temperature. Both heat treatment processes are illustrated schematically in Fig. 2. It should be noted that the annealing and T6-strengthening processes were carried out by ERG, Oakland CA.

Following fabrication and processing, foams were sectioned and sandwiched using Al face sheets. A typical sandwich specimen is shown in Fig. 3a. The top and bottom Al face sheets were bonded to foam core using epoxy. The sandwich dimensions are ∼71.1 (L) mm ×58.4 (W) mm ×75.0 (H) mm. Since the thickness of each face sheet is about 2.6 mm, the foam core has a height of ∼69.8 mm. A prior study [18] showed that the attached bottom and face sheets did not affect the foam strength and deformation under monotonic and cyclic compression. Thus, the foam strengths were measured using such foam sandwiches.

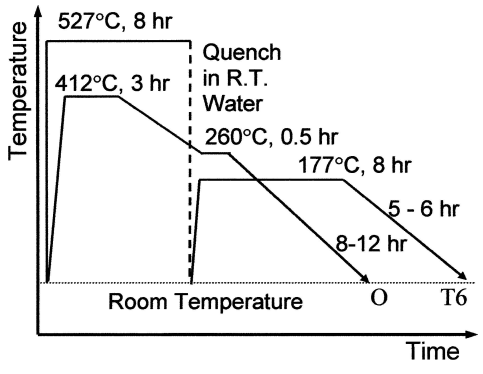

Figure 2 Schematic diagram of the annealing (O) and T6-strengthening (T6) processes.

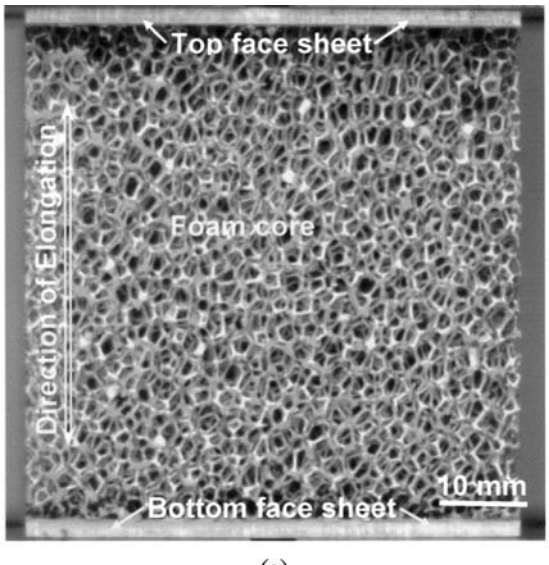

(a)

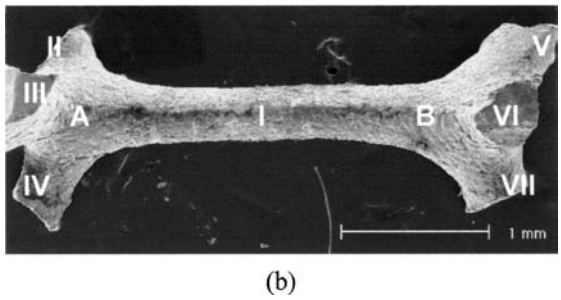

(b)

Figure 3 A typical foam sandwich with attached top and bottom Al face sheets. The dimensions of the shown foam block are of 58.00 × 71.00 × 69.80 mm. (b) A strut extracted from foam sandwich using EDM.

3. Experimental procedures

3.1. Strut extraction

Individual struts were extracted from foam sandwiches in the three heat treatment conditions (F, O and T6).

This was done using a two-step EDM process. First, 2-mm-thick foam slices were cut from foam blocks (Fig. 3b) using a wire EDM at Xact Wire EDM Corporation, Waukesha WI. Then, the individual struts were detached from the 2-mm-thick foam slices using a ram-type Uni-tek US EDM Model D-55 system (Uni-tek Manufacturing Company, Frankfort, IL). The extracted struts were cleaned in acetone. Since struts may have non-uniform shapes that are not representative of the typical strut geometry, a number of struts were extracted and cleaned, but only a few of them were selected for micro-tensile testing.

3.2. Fixture design

A typical strut (Fig. 3b) does not have a regular dog-bone geometry. The two ends of the strut correspond to two vertices (Vertices A and B). Each vertex is a joint of four struts: vertex A is the joint consisting of struts I, II, III and IV; while vertex B is the joint consisting of struts I, V, VI and VII. Struts II–VII were cut to separate strut I from the foam matrix. The vertex thickness is significantly greater than those of the struts. Such a structure is difficult to load using conventional tensile loding fixture. In this study, two special grips were designed to fix the struts, and apply tensile loads during micro-tensile testing.

A schematic illustration of the loading fixture that was designed is shown in Fig. 4a. The gripper consists of an inclined loading segment that resembles the nail-puller side of a claw hammer. For alignment along the longitudinal axis, both the right and left grippers share the same longitudinal axis. The inclination is in the transverse direction to facilitate the "seating" of the specimen. The inclined puller contains a slot that shares the same axis of symmetry as the inclined puller. The slot has an opening angle of 60°, and the slot depth is 2 mm. This geometry enables the gripping of the struts at locations close to the two vertices. In this way, there was no need for a pre-load prior to micro-tensile testing. A typical image of an undeformed strut is presented in Fig. 4b. This displays a strut sitting between two grippers. The image was obtained using scanning electron microscopy (SEM) prior to micro-tensile testing.

3.3. Engineering stress calculation

To calculate the engineering stress, the cross sectional area of each strut should be measured before testing. A prior study [13] revealed that the cross section of a strut in Duocel® open cell aluminum foams was triangular in shape, as shown in Fig. 4c. The coat-like substance surrounding the strut cross section in Fig. 4c is a transition layer from hard strut alloy to soft epoxy layer, which was used to cold mount foam samples for grinding and polishing. The transition layer was formed during grinding and polishing. In the triangular cross section of the strut, each of the three edges corresponds to the cross section of the three strut faces. Thus, the lengths of the three edges ($a_{\bar{1}}$, $a_{\bar{2}}$ and $a_{\bar{3}}$) are actually the widths of the three corresponding strut faces. Hence, the edge lengths were obtained by measuring the corresponding face widths. The face widths of a strut were measured using

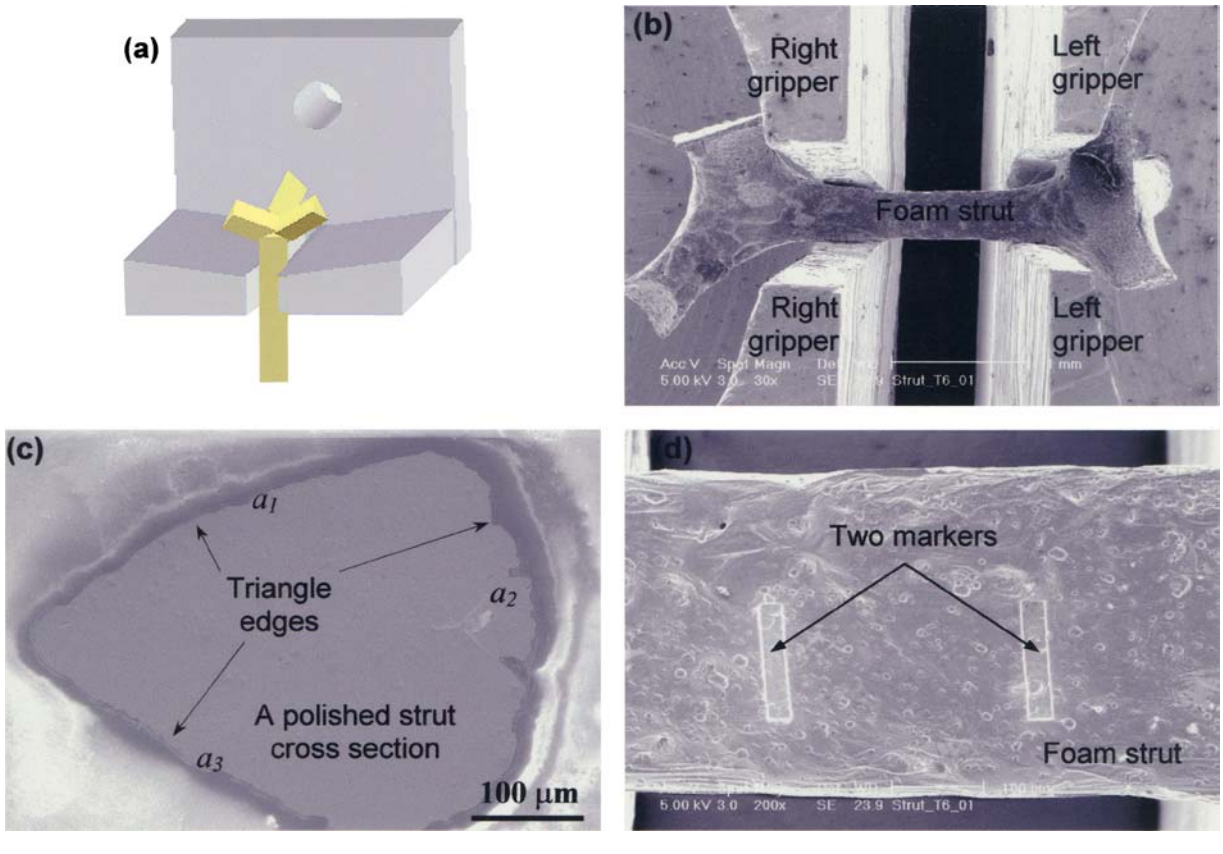

Figure 4 (a) Schematic illustration of a designed gripper containing a inclined puller with a slot for strut gripping. (b) A strut sitting in the left and right grippers before a microscale tension testing. (c) The strut cross section is triangular in shape. (d) Two markers on the strut surface.

focused ion beam (FIB) microscopy in the electron beam mode. The FIB microscope allows considerable rotation angle (up to 52°), to align the strut such that the normal of any of the three strut faces is parallel to the injection electron beam. The measurements were carried out using a reference object with known dimensions for calibration.

Since the widths of a strut face vary along their longitudinal axis, multiple measurements (more than 30) were performed in the gauge length, where the surface markers would be, to obtain representative value for each strut face. The average value was used as the corresponding edge length of the cross section, i.e.

$$a_{\mathrm{i}} = \frac{1}{N}\sum_{\mathrm{j}}^{\mathrm{N}} a_{\mathrm{ij}} \quad i = 1, 2, 3 \tag{2}$$

where a_{ij} is the jth measured individual face width value, and N is the number of measurements. The average width values calculated using Equation 2 were ∼300–450 μm. These were consistent with the prior results [13]. The initial cross section area of the strut, S_0, was then calculated from the following equation:

$$S_0 = \frac{1}{4}\sqrt{4a_1^2a_3^2 - \left(a_1^2 + a_3^2 + a_2^2\right)^2} \tag{3}$$

The initial cross section area of the strut obtained from Equation 3 was used subsequently to calculate the engineering stress values.

3.4. Engineering strain measurement

Engineering strain was measured using a non-contact technique, which involved using surface markers on the strut surfaces. By measuring the distance changes between surface markers during micro-tensile testing, the engineering strains can be calculated. The surface markers were made using ion-beam induced sputter etching in the FIB microscopy. They have a rectangular shape with widths of ∼20 μm, lengths of ∼120 μm and depths of ∼3.0 μm. Multiple markers were made along the strut axis. The distance between the markers was about 300 μm. Two rectangular markers are shown clearly in Fig. 4d.

During micro-tensile testing, *in situ* digital images were recorded, and the images were then processed using the VisionBuilder™ program from National Instruments, Austin, TX. This starts by creating landmarks on the strut in regions containing surface markers. These landmarks were then used in the pattern recognition processes. Batch processing of the *in situ* images was used to determine the locations of the landmarks in the x and y directions. The distances between landmarks were calculated from their current coordinates, engineering strains were thenafter calculated from the distance changes between landmarks.

3.5. Microscale tensile testing

Microscale tensile tests of struts were performed in a system that was developed for MEMS structure testing [19]. The system is based on an original design by Sharpe *et al.* (Johns Hopkins University) [20]. Fig. 5 shows a schematic and a photograph of the micro-tensile testing system. The system includes a unislide drive (Velmex, Inc., Bloomfield, NY) attached to a load cell (Entran, Fairfield, NJ) and the grips that are used to load the specimens between two platforms (one stationary and one mobile). Micropositioners were used to ensure the alignment of the loading axis, load cell and gripping system. The load cell was connected to the unislide on one side, and to a frictionless Nelson air bearing (Nelson Air Corp., Milford, NH) on the other side. The mobile platform was mounted on the sliding shaft of the bearing.

The load cell was calibrated before each testing, using several known loads. The unislide drive provided a displacement control mode, with a constant strain rate of 5×10^{-4} s^{-1}. A CCD camera was used to capture *in situ* images of the deforming specimen. These were recorded on the hard drive of a PC, along with the load data. Both image and load data acquisition were synchronized using Labview™ and IMAQ Vision software (IMAQ Vision and Labview™ are trademarks of National Instruments, Austin, TX). The frequency of image and data recording was 5 Hz. The stress-strain curves were obtained from the load and displacement data.

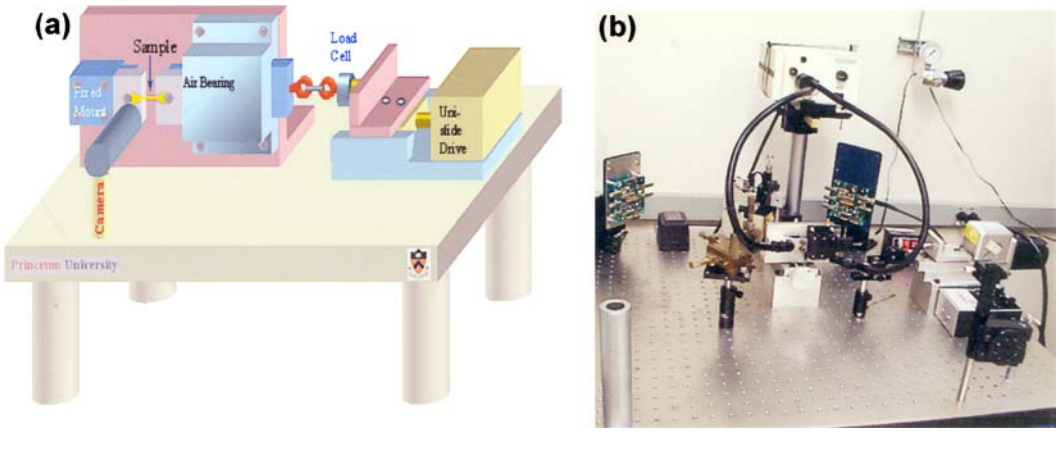

Figure 5 A schematic diagram (a) and a photo (b) of the micro-tensile testing system for strut testing.

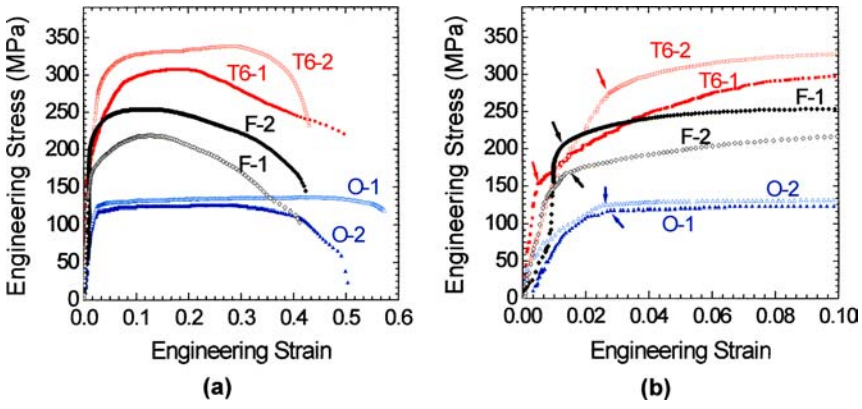

Figure 6 Stress-strain curves of the struts under the three conditions (F, O and T6): (a) complete stress-strain curves; and (b) stress-strain curves plotted in a smaller scale.

4. Results

4.1. Tensile properties of the struts and the corresponding bulk alloys

For each heat treatment condition (F, O and T6), the micro-tensile testing was performed on two struts. The measured stress-strain curves are presented in Fig. 6. The slopes of the stress-strain curves in the initial deformation regime were much lower than the typical Young's moduli (70 GPa) of aluminum alloys, and the 0.2% offset yield point does not corresponds to the onset of the plastic deformation. However, abrupt slope change was observed in each measured stress-strain curve. These critical points corresponding to the abruptslope change were indicated using arrows in Fig. 6b. In this study, these critical points were defined as the yield points. The stress and strain of these critical points are summarized in Table II, along with the ultimate tensile strength (UTS) values. Also included in Table II are values of the ductility corresponds to the total strain to fracture for each strut.

The two as-fabricated struts had similar yielding and plastic flow behavior. The yield strain levels were ∼0.011 and ∼0.013, and the corresponding yield strengths were 188 and 157 MPa for strut F-1 and F-2, respectively. Similarly, the UTS values obtained for the two struts were 247 and 207 MPa for struts F-1 and F-2, respectively. Struts F-1 and F-2 failed respectively at strain levels of 0.431 and 0.441.

Compared to the as-fabricated struts, the T6-strengthened struts had significantly higher strengths. The UTS values of struts T6-1 and T6-2 were 307 and 338 MPa, respectively. The yield strength of strut T6-2 was 285 MPa. However, the yield strength of strut T6-1 was only 153 MPa. This value was even lower than the strengths of the as-fabricated struts. The reasons for this will be discussed in the succeeding sections. It is worth noting that the T6-strengthening did not impair the ductility of the struts. The fracture strains were 0.400 and 0.431 for struts T6-1 and T6-2, respectively. These are comparable to those of the as-fabricated struts (Table II).

The two annealed struts had surprisingly similar tensile stress-strain behavior. Corresponding to the critical yielding points, struts O-1 and O-2 had similar stain of ∼0.023. The yield strengths were 111 MPa and 120 MPa, respectively for the two struts. The UTS values for struts O-1 and O-2 were 125 MPa and 136 MPa, while the fracture strains of the two annealed struts O-1 and O-2 were ∼0.491 and 0.573, respectively. These are significantly greater than those of the as-fabricated and T6-strengthened struts. Furthermore, the annealed struts exhibited nearly elastic-perfectly plastic behavior with very little strain hardening.

It is clear that annealing reduces strut strength, but improves strut ductility. It also results in nearly elastic-perfectly plastic stress-strain behavior. In the case of the T6-strengthened struts, the measured UTS values increase, but strengthening is not associated with degradation in strut ductility. Furthermore, all tested struts had good ductility between 40 to 60% (Table II).

For a comparison, efforts had been taken to measure the tensile properties of the corresponding fully-dense 6101 aluminum subjected to the same heat treatment conditions (F, O and T6). The ∼0.5 mm thick aluminum films seriously deformed after being sliced from the

TABLE II Tensile properties of the struts under F, O and T6 conditions

Specimen ID	Linear elastic limit		UTS		Breaking point	
	Strain	Stress MPa	Strain	Stress MPa	Strain	Stress MPa
F-1	0.011	188.36	0.104	247.37	0.431	140.34
F-2	0.013	156.54	0.109	206.70	0.441	86.48
O-1	0.024	111.23	0.294	124.63	0.491	58.76
O-2	0.023	119.66	0.414	135.71	0.573	118.75
T6-1	0.019	200.08	0.180	306.77	0.400	256.61
T6-2	0.031	284.89	0.270	338.17	0.431	232.87

TABLE III Tensile properties of 6101 the bulk alloys under F, O and T6 conditions

Specimen ID	0.2% offset yield point		UTS		Breaking point	
	Strain	Stress MPa	Strain	Stress MPa	Strain	Stress MPa
F-1	0.003	98.00	0.161	174.52	0.305	126.19
F-2	0.003	98.00	0.184	173.84	0.336	143.59
O-1	0.003	45.64	0.194	88.54	0.554	59.26
O-2	0.003	49.00	0.227	87.79	0.304	57.56
T6-1	0.005	192.50	0.046	205.32	0.064	184.01
T6-2	0.005	199.50	0.024	209.87	0.029	186.97

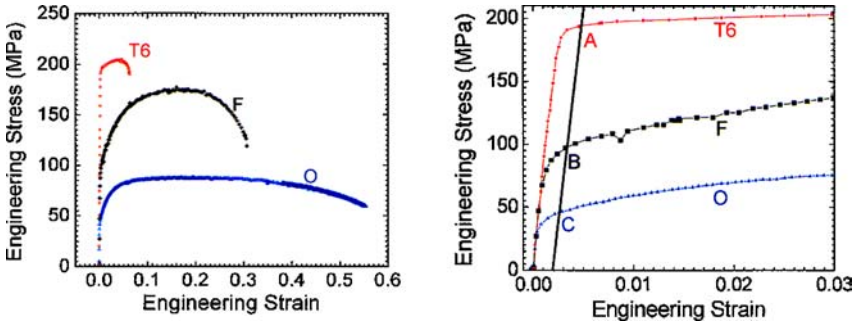

Figure 7 Stress-strain curves measured using tensile specimens with gauge cross section of 5.0 × 10.0 mm, and gauge length of 50.0 mm: (a) typical stress-strain curves for 6101 bulk alloys under three conditions (F, O and T6); and (b) the onset of yielding corresponding to the 0.2% offset yield strength.

bulk alloy using EDM. Thus, macro-scale testing was carried out on dogbone tensile specimens with a gauge cross section of 5.0×10.0 mm, and a gauge length of 50.0 mm. The specimens were deformed continuously to fracture at a strain rate of 5×10^{-4} s^{-1}. The results are summarized in Table III. Typical stress-strain curves are presented in Fig. 7a. In the case of the as-fabricated bulk alloy, the 0.2% offset yield strength and UTS are ∼98 MPa and ∼174 MPa, respectively. The plastic strain to failure is about 30 percent. The T6-strengthening process doubles the 0.2% offset yield strength, but leads to only a limited increase in the UTS, from ∼174 MPa for the as-fabricated alloy to ∼205 MPa for the T6-strengthened alloy. However, the T6-strengthening process significantly impairs the ductility of the bulk alloy, which failed at a strain less than 6 percent. The plasticity of bulk alloy was significantly improved to more than 50 percent by annealing, but both the 0.2% offset yield strength and UTS values of the annealed alloys were reduced to about half of the corresponding strengths of the as-fabricated alloy. In Fig. 7b, stress-strain curves are plotted in small strain scale. The onset of yielding was estimated by drawing a line that starts from a point on the strain axis with a strain of 0.2%. The slope of the drawn line was 70 GPa, which was the Young's modulus of the aluminum alloy. The onset of yielding was denoted by points A, B and C in the corresponding curves that were obtained in the bulk alloy in the three conditions (F, O and T6).

4.2. Strut deformation

Fig. 8 presents the selected *in situ* images showing the deformation sequence of an as-fabricated strut during testing. Following the application of a tensile load, the strut started sliding in the slots of the two grippers. A very low load was enough to translate the strut in a direction that was parallel to the loading axis. No distance change was observed between the three markers (Fig. 8a), which were denoted as 1, 2 and 3. After the two vertices met the outside wall of the two grippers, the increasing load caused elastic deformation. The strut was then clamped, and plastic deformation soon began, with the visible evidence of shear banding becoming apparent at a strain of 0.019 (Fig. 8b). Further plastic deformation led to geometrical instability, with necking being observed at strains between 0.038 and 0.167 (Fig. 8c and d). The strut sustained loads up to a strain of 0.384, without breaking (Fig. 8f). Significant shear bands were also observed to extend across the strut thickness during microscale tension testing (Fig. 8c–f).

4.3. Strut fracture

Two types of fracture modes were observed in the fractured struts. These are shown in Fig. 9. The two parts (parts I and II) of a fractured strut are presented in Fig. 9a. The fracture surfaces were labeled, along with the impressions that were made by grippers in the vertices during testing. The fracture surface of part II was amplified in Fig. 9b. Fracture occurred in two facets that were perpendicular to each other. We believe that the two perpendicular facets were formed due to grain boundary shearing. Such a fracture mode was defined as fracture mode I. Since it involved grain boundary shearing, it was an intergranular fracture mode. Fracture may occur within a single grain, as shown in Fig. 9c and d. This involved stable tearing mechanisms that give rise to "striation" that form closed loops around the circumference of the strut (Fig. 9c). High magnification SEM

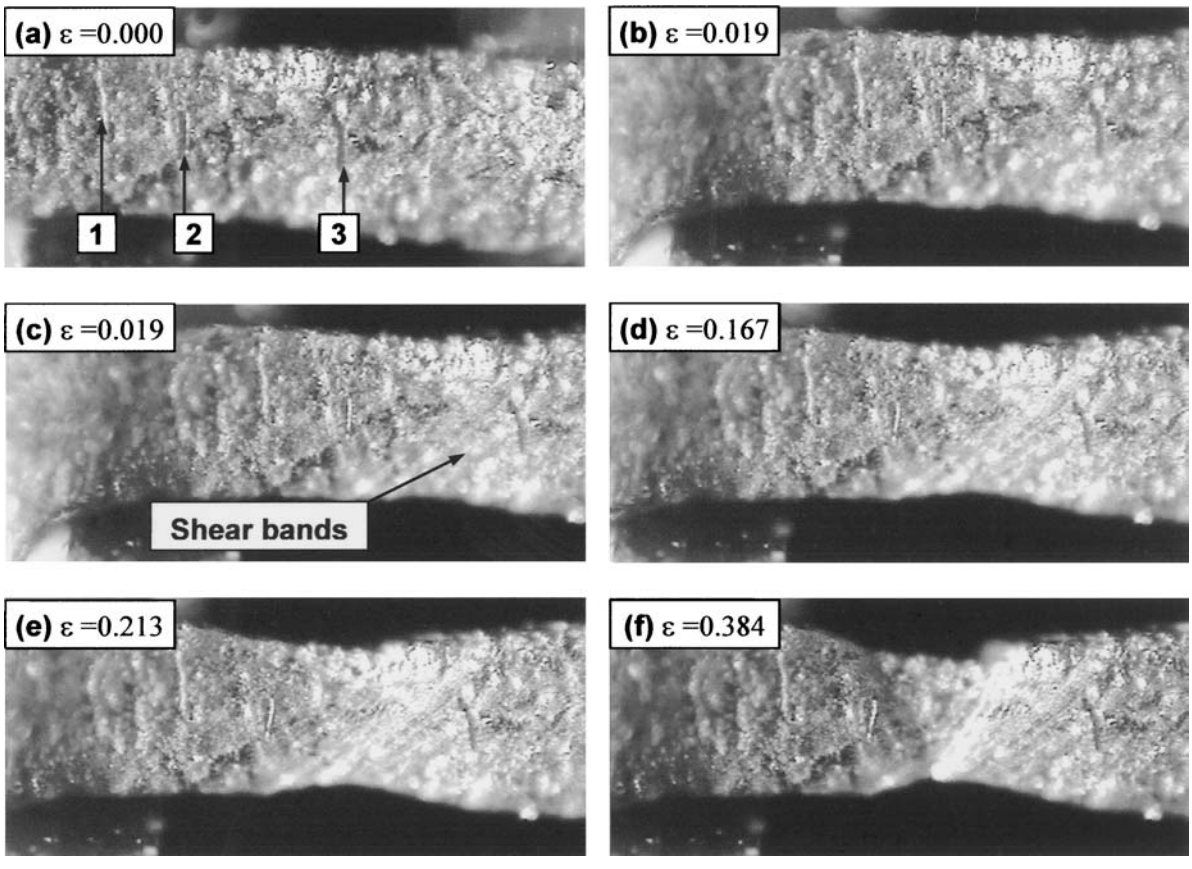

Figure 8 Deformation sequence of an as-fabricated strut (F-2) during microscale tension testing. The three markers on the strut surface are indicated in image (a).

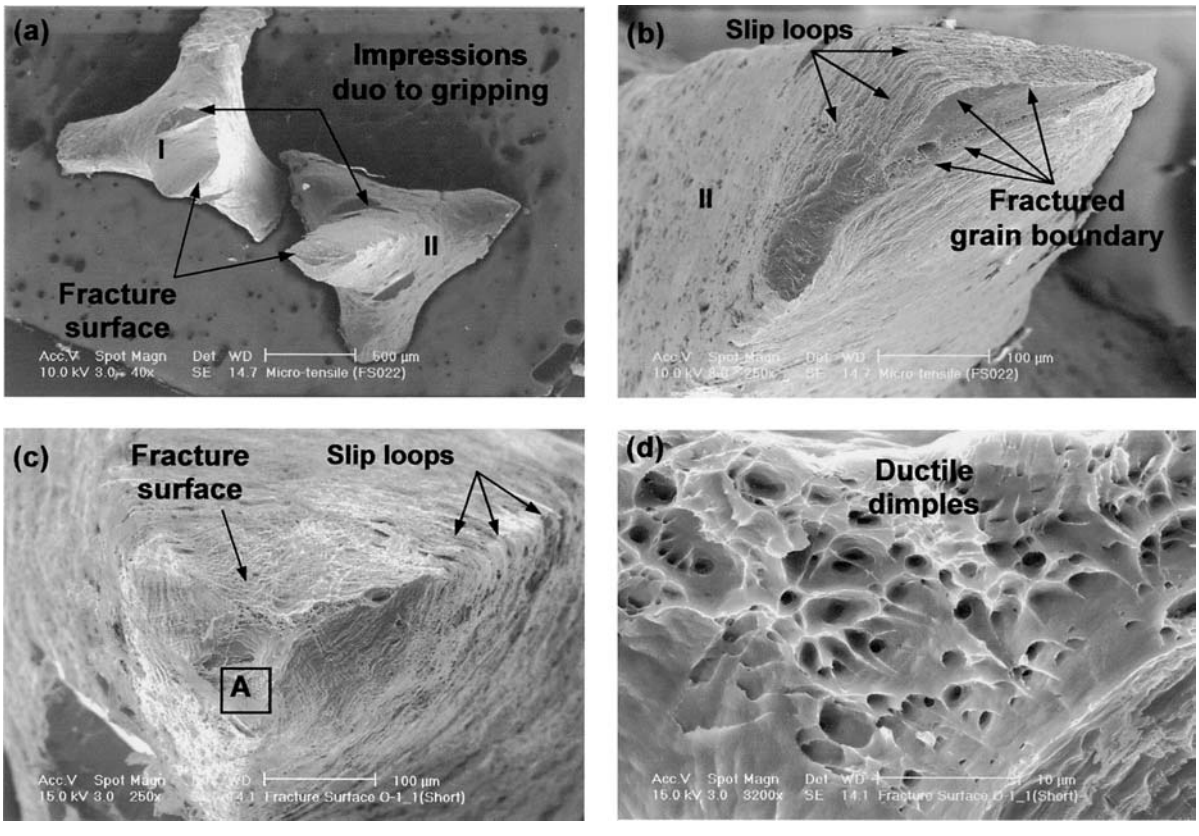

Figure 9 Fracture surface of an annealed struts after microscale tension testing: (a) two broken parts of the tested strut; (b) grain boundary shearing was observed in part II; (c) fracture surface and parallel slip loops around the circumference of another tested strut; and (d) ductile dimples in the selected region A on the fracture surface in (c).

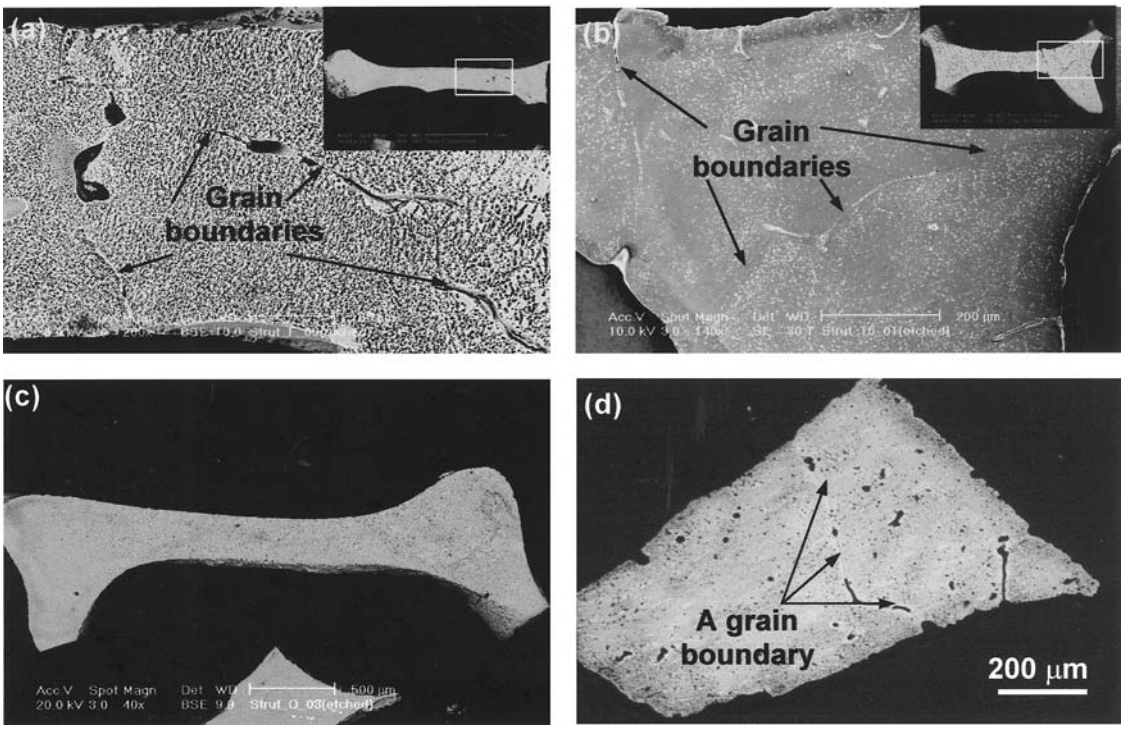

Figure 10 Bamboo grain structures in polished struts etched with modified Keller Reagent: (a) the grain structure of a strut in the as-fabricated condition; (b) grain structure of a strut in the T6-strengthened condition; (c) no grain boundary was observed in a strut in the annealed condition; and (d) a through-thickness grain boundary in an annealed strut.

images also revealed clear evidence of transgranular ductile dimpled fracture. The second type of fracture was denoted as type II. Hence, both types I and II fracture involve significant plastic deformation, prior to the onset of failure.

5. Discussion

5.1. The strut properties and grain structure

The measured strut stress-strain curves (Fig. 6) showed that the strain levels corresponding to the critical points were typically greater than 0.01, which was significantly greater than the strain levels (typically between 0.003–0.005) corresponding to the 0.2% offset yield strengths obtained from the bulk 6101 alloy (Fig. 7). This may be associated with the actual strut geometry. The strut curvature was evident in Fig. 1, in which most struts have initial curvature. Similar curvature was observed and studied in prior studies [21, 22]. During micro-tensile testing, the struts were first straightened up by bending before uniaxial tension. Such bending resulted in significant reduction in strut stiffness. The small slopes of the linear elastic portion of the measured strut stress-strain curves (Fig. 6) are at least partially attributed to the initial strut curvature. Since the extent of bending deformation depends on the curvature levels, the strut curvatures may also be one of the reasons to cause significant difference in the measured stress-strain curves for the two struts under the same heat treatment conditions (Table II). Furthermore, the erratic behavior in initial deformation stage was observed in the measured stress-strain curves. This may be attributed to the initial motion of the specimen before it becomes fully seated in the grips. Nevertheless, the strut microstructure must be another important factor, along with the initial strut curvature, to affect the strut stress-strain behavior.

The grain structures of individual struts are presented in Fig. 10a–d. The grain boundaries were displayed by etching the polished struts using modified Keller Reagent [13]. Fig. 10a displays grain boundaries in a strut in the as-fabricated condition. A grain boundary perpendicular to strut surface was observed across the strut thickness. Moreover, grain boundaries were only observed in the regions indicated by the rectangle in the figure inset, which displays the microstructure of the overall strut transverse section. Thus, this strut exhibits a typical bamboo grain structure. Similar bamboo grain structure was also observed in a T6-strengthened strut (Fig. 10b). Grain boundaries only presented in the region indicated by the rectangle in the figure inset, with a grain boundary across the strut thickness. No grain boundaries were observed in a selected strut in annealing condition (Fig. 10c). However, a through-thickness grain boundary was observed in another selected strut in annealed condition (Fig. 10d). These observations suggest that a typical strut consists of one grain or has bamboo grain structure, and the grain structure in not affected by heat treatments.

Such strut grain structure is consistent with the *in situ* strut deformation observations (Fig. 8) and the fracture analysis (Fig. 9). The through-thickness shear bands in Fig. 8 indicate that the deformation of the strut occurs within one grain. Despite the two types of fracture modes (types I and II) displayed in Fig. 9, significant deformation occurs in the constituent grains.

In case of struts containing single crystal or having bamboo grain structure, the measured strut stress-strain curves may correspond to the deformation of

face-centered cubic single crystals. The critical resolved shear stress for annealed pure aluminum single crystal is only ~1 MPa, which is only one percent of the measured strut strengths (Table II). However, the stress-strain characteristics and strengths of single crystals are determined by several factors, among which are the size of specimen, purity of the metals and crystalline orientation to the load axis [23]. Compared to pure aluminum (with typical purity of 99.996), the 6101 alloy contains much more alloy elements that contribute to alloy strengthening, along with the precipitate strengthening due to heat treatment. Furthermore, it has been reported that the surface oxide scale resulted in significant strengthening effect [24, 25] for samples with diameter of about 10 mm. The strengthening effect is expected to be more predominant for foam struts that have diameter less than 0.5 mm. Future studies are required to quantitatively investigate these strengthening effects.

5.2. Estimation of foam strength

After measuring the mechanical properties of the struts and the corresponding bulk alloy, we are ready to estimate the plastic collapse strengths of foams, and evaluate how the measured strut properties affect the foam strength predictions. This is done by incorporating the measured strengths of the struts and the corresponding bulk alloy subjected to the same annealing process, along with nominal yield strength of the annealed bulk alloy (75 MPa) [16], into the Gibson and Ashby model [1] to predict the foam strengths. The predictions are plotted in Fig. 11, as well as the measured strengths obtained from the annealed foams. The foam strengths predicted from the measured and nominal yield strengths of the bulk alloy are significantly lower than those predicted from the measured foam strengths. The predictions from the measured strut strengths are still less than, but closer to the measured foam strengths.

Fig. 11 indicates that the measured foam strengths distribute in ranges, instead of a single value. To accommodate this phenomenon, a four-strut structure unit model was proposed to contain the structure parameters in Duocel® open cell foams, and the strength bounds

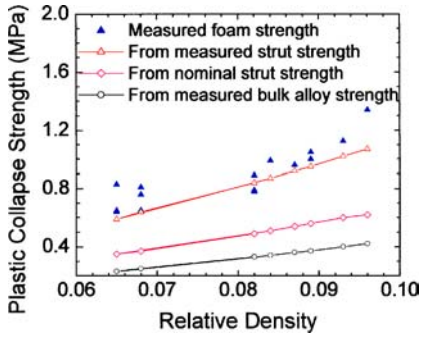

Figure 11 Comparisons between measured and predicted strength of annealed foams. Annealed foam strengths are predicted from the directly measured strut strength, measured strength of the corresponding bulk alloy under same heat treatment condition, and the corresponding nominal strength from handbooks [17].

were predicted via the following formula [7]:

$$0.31\sigma_{YS}\left(\frac{\rho_f}{\rho_s}\right)^{3/2} \le \sigma_{pl}^{cl} \le 0.44\,\sigma_{YS}\left(\frac{\rho_f}{\rho_s}\right)^{3/2} \qquad (4)$$

where the variables have been introduced in Equation 1. A comparison of the two model predictions is presented in Fig. 12, along with the strengths measured from foams under the three heat treatments. The comparison suggests that the directly measured mechanical properties of individual strut are required to accurately predict the foam strength.

5.3. Implications

This study clearly shows that measured strut properties are significantly different from the mechanical properties of the corresponding bulk alloy subjected to the same heat treatment. They are also different from the nominal properties that are found in a handbook [17]. These different strut strengths result in different estimations of foam strengths. Hence, the strut properties should be directly measured to ensure precise predictions.

The micro-scale tensile testing system is a good candidate for such measurements, since it is designed for small structure testing. The specially designed grips take advantage of the factor that the diameters of the vertices are greater than those of the struts. Before tensile load is applied, the strut is allowed to be seated in the slots and supported by the two grips. No fixtures are needed to prevent strut movement. In contrast, strut sliding is allowed and encouraged to clamp strut in grippers after tensile load is applied. Since strain is measured using *in situ* image sets, the translation of struts before clamping does not affect strain measurements.

However, the initial deformation was not correctly measured due to two factors. The first one is the initial strut curvature. The second factor is about the strain measurement. Laser fringe patterns can be used to measure strain at high resolution [20]. However, the rough strut surfaces prevent using laser fringe patterns to measure the strains. These two factors seem to be overcome by preparing struts with polished surfaces, but it is not practical since deformation would be introduced during preparing and manipulating strut specimens.

It is important to note that only a limited number of struts were selected and tested in this study. They are not enough to provide a statistical understanding of the mechanical behavior of individual struts in aluminum open cell foams. Therefore, multiple tests are needed in future study. Furthermore, the deformation of struts in foam block is most likely to be caused by compression or bending. Thus, compression and bending tests on single struts may provide more information to understand foam deformation. However, the difficulty of compression or bending tests is how to control the boundary conditions. It is also a challenge to mimic real boundary conditions of foam struts during deformation, because deformation may occurs simultaneously on numerous

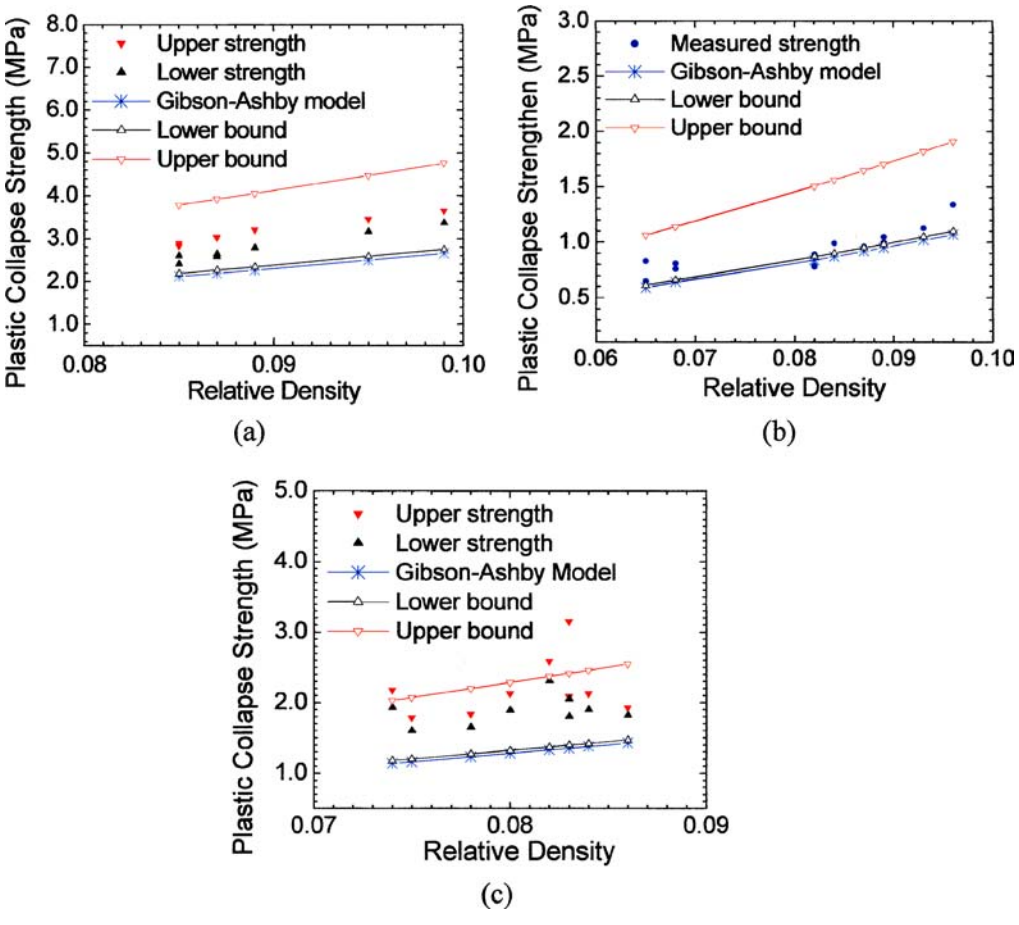

Figure 12 Comparisons between the measured foam strengths and the predicted strengths using Gibson-Ashby cubic model and the four-strut unit cell model. The measured strut strenghs are used to make predictions: (a) the annealed foams; (b) T6-strengthened foams; and (c) the as-fabricated foams.

struts, and deformation of these struts would affect each other.

6. Summary and concluding remarks

In this study, micro-tensile testing was performed on struts that were extracted from open cell aluminum foams in the as-fabricated (F), annealed (O) and T6-strengthened (T6) conditions. The measured strut properties reveal that strut tensile strength and ductility are significantly greater than those of the corresponding bulk alloy subjected to the same heat treatment conditions. Since the strut curvature significantly reduces the strut stiffness, the critical point where the slope of the stress-strain curve changes abruptly is defined as the yielding point, and the strut yield strengths are obtained accordingly. Such yield strengths are used to estimate the foam plastic collapse strengths using the Gibson-Ashby dimensional model and the four-strut unit cell model. A comparison of the predicted and measured foam strengths suggests that direct measurements of strut strengths are critical for accurate predictions of foam strength.

Acknowledgements

This research was supported by the Office of Naval Research (ONR). The authors would like to thank the ONR Program Manager, Dr. Julie Christodolous, for her encouragement and support. Appreciation is also extended to Prof. Anthony Evans, Prof. Zhigang Suo and Prof. Alberto Cuitiño for stimulating discussions on the fatigue of metals foams. Grateful thanks and acknowledgements are due to Mr. Bryan Leyda of ERG, for his assistance with foam processing and heat treatment. Finally, the authors would like to thank Dr. George Yoder, formerly of ONR, for his assistance in the initiation of this work.

References

1. L. J. GIBSON and M. F. ASHBY, "Cellular Solids: Structure and Properties," 2nd ed. (Cambridge, UK, Cambridge University Press, 1997).
2. Y. WANG and A. M. CUITINO, *J. Mechanicas and Phys. Solids* **48** (2000) 961.
3. T. G. NIEH, K. HIGASHI and J. WADSWORTH, *Mater. Sci. Engng*. A **283A** (2000) 105.
4. G. GIOIA, Y. WANG and A. M. CUITIÑO, *Proceedings of the Royal Society of London* A **457** (2001) 1079.
5. C. SAN MARCHI and A. MORTENSEN, *Acta Materialia* **49** (2001) 3959.
6. Y. W. KWON, R. E. COOKE and C. PARK, *Mater. Sci. Engng.* A **343** (2003) 63.
7. J. ZHOU and W. O. SOBOYEJO, *Engng. Manufacture and Materials*, 2003 (accepted for publication).
8. M.F. ASHBY, A. G. EVANS, N. A. FLECK, L. J. GIBSON, J. W. HUTCHINSON and H. N. G. WADLEY, "Metal Foams—A Design Guide" (Butterworths Heinemann, London, UK, 2000).
9. J. BANHART, *Progress in Materials Science* **46** (2001) 559.
10. V. GERGELY, R. L. JONES and W. CLYNE, *Transactions of JWRL* **30** (2001) 371.

11. A. E. MARKAKI and T. W. CLYNE, *Acta Materialia* **49** (2001) 1677.
12. A. E. SIMONE and L. J. GIBSON, *ibid.* **46** (1998) 3109.
13. J. ZHOU, C. MERCER, and W. O. SOBOYEJO, *Metall. Mater. Transactions* A **33** (2002) 1413.
14. D. LEHMHUS, C. MARSCHNER and J. BANHART, *J. Mater. Sci.* **37** (2002) 3447.
15. D. LEHMHUS, J. BANHART and M. A. RODRIGUEZ-OEREZ, *Mater. Sci. Tech.* **18**(1) (2002) 1.
16. J. ZHOU, S. ALLAMEH and W. O. SOBOYEJO, in Proceedings of the J. F. Knott Symposium: Mechanics of Fracture, edited by W. O. Soboyejo, J. J. Lewandowski, and R. O. Ritchie (TMS Fall Meeting, Columbus, OH, 2002) p. 199.
17. "ASM Metal Handbook" (ASM International, 1990, USA) Vol. 2.
18. A.-M. HARTE, N. A. FLECK and M. F. ASHBY, *Acta Materialia* **47** (1999) 2511.
19. P. SHROTRIYA, S. M. ALLAMEH, J. LOU, T. BUCHEIT and W. O. SOBOYEJO, *Mechanics and Mater. J.* (2001) (Submitted).
20. W. N. SHARPE, JR., B. YUAN, R. VAIDYANATHAN and R. L. EDWARDS, in Proceedings of the SPIE Symposium on Micolithography and Metrology in Micromachining II (Austin, TX, 1996) p. 78.
21. E. ANDREWS, W. SANDERS and L. J. GIBSON, *Mater. Sci. Engng.* A **A270** (1999) 113.
22. A. E. SIMONE and L. J. GIBSON, *Acta Materialia* **46** (1998), 3929.
23. R. ABBASCHIAN and R. E. REED-HILL, "Physical Metallurgy Principles," 2nd ed. (PWS Publishing Company, Boston, MA, 1994).
24. E. N. DAC. ANDRADE and C. HENDERSON, *Math. Physical Sci.* **244** (1951) 177.
25. F. D. ROSI and C. H. MATHEWSON, *Transaction of the AIME* **188** (1950) 1159.

Received 16 June 2003
and accepted 12 March 2004